CrossMark

RESEARCH PAPER

3D v_P and v_S models of southeastern margin of the Tibetan plateau from joint inversion of body-wave arrival times and surface-wave dispersion data

Lina Gao · Haijiang Zhang · Huajian Yao · Hui Huang

Abstract A new 3D velocity model of the crust and upper mantle in the southeastern (SE) margin of the Tibetan plateau was obtained by joint inversion of body- and surface-wave data. For the body-wave data, we used 7190 events recorded by 102 stations in the SE margin of the Tibetan plateau. The surface-wave data consist of Rayleigh wave phase velocity dispersion curves obtained from ambient noise cross-correlation analysis recorded by a dense array in the SE margin of the Tibetan plateau. The joint inversion clearly improves the v_S model because it is constrained by both data types. The results show that at around 10 km depth there are two low-velocity anomalies embedded within three high-velocity bodies along the Longmenshan fault system. These high-velocity bodies correspond well with the Precambrian massifs, and the two located to the northeast of 2013 M_S 7.0 Lushan earthquake are associated with high fault slip areas during the 2008 Wenchuan earthquake. The aftershock gap between 2013 Lushan earthquake and 2008 Wenchuan earthquake is associated with low-velocity anomalies, which also acts as a barrier zone for ruptures of two earthquakes. Generally large earthquakes ($M \geq 5$) in the region occurring from 2008 to 2015 are located around the high-velocity zones, indicating that they may act as asperities for these large earthquakes. Joint inversion results also clearly show that there exist low-velocity or weak zones in the mid-lower crust, which are not evenly distributed beneath the SE margin of Tibetan plateau.

Keywords Joint inversion · Body waves · Surface waves · Aftershock gap · The southeastern margin of Tibetan plateau

L. Gao
School of Geoexploration Science and Technology, Jilin University, Changchun 130026, China
e-mail: gaolina19910926@sina.com

L. Gao · H. Zhang (✉) · H. Yao
Laboratory of Seismology and Physics of Earth's Interior, School of Earth and Space Sciences, University of Science and Technology of China, Hefei, Anhui, China
e-mail: zhang11@ustc.edu.cn

H. Zhang · H. Yao
National Geophysical Observatory at Mengcheng, Mengcheng, Anhui, China

H. Huang
Department of Earth, Atmospheric and Planetary Sciences, Massachusetts Institute of Technology, Cambridge, MA, USA

Present Address:
H. Huang
Compagnie Générale de Géophysique, Houston, Texas, USA

1 Introduction

The uplift and expansion of the Tibetan plateau (TP) are the result of the Indian-Eurasian collision since ∼50 million years ago (e.g., Yin and Harrison 2000; Royden et al. 1997, 2008). Despite many studies in the past (e.g., Molnar and Tapponnier 1975; Tapponnier et al. 1982; Royden et al. 1997; Liu et al. 2014), the uplift and deformation of the TP are still controversial. The southeastern (SE) margin of the TP is one of the key areas for understanding the tectonic evolution of the plateau. Adjacent to the Sichuan basin, the Longmenshan (LMS) rises about 5000 m above the Sichuan basin within a range of 50 km and is the steepest margin, whereas the SE margin toward Yunnan is gentle. Across the LMS, the crustal thickness also greatly

varies from ∼60 km in the west to ∼40 km in the east (Zhang et al. 2009, 2010). However, the eastern margin lacks large-scale young crustal shortening structures (Shen et al. 2005). Two models have been proposed to explain how the LMS is formed: (1) crustal shortening and thickening model, in which extrusion along the lateral strike-slip faults caused by the subduction of Asian lithospheric mantle results in crustal shortening and uplift of the LMS (Tapponnier et al. 2001); (2) crustal channel flow model, in which eastward ductile mid-crustal flow is obstructed by the rigid Sichuan basin (Royden et al. 1997). An important difference between these two models is whether crust and mantle of the eastern plateau are decoupled. The high-resolution velocity models from tomography can provide more constraints on these different models.

According to Shen et al. (2005), the SE margin of the TP can be divided into several blocks. The lateral variation in the crustal strength of the blocks and interaction between blocks make this area one of the most active seismic regions in China. The 2008 Wenchuan earthquake and the 2013 Lushan earthquake occurred on the Longmenshan fault (LMSF) system. Notably, there is an obvious aftershock gap of about 35 km in length between the Wenchuan and Lushan earthquakes (Xu et al. 2013). Previous tomography results have shown a clear low-v anomaly in the gap in the crust (e.g., Lei and Zhao 2009; Lei et al. 2014; Pei et al. 2014; Wang et al. 2015).

Previously, extensive geophysical imaging studies have been conducted in the SE margin of the TP, including magnetotelluric imaging (Bai et al. 2010; Zhao et al. 2012), seismic body-wave tomography (Pei et al. 2010, 2014; Wang et al. 2009, 2015; Zhang et al. 2012), surface-wave tomography (Li et al. 2009; Huang 2014; Yao et al. 2008; Yao 2012), receiver function analysis (Xu et al. 2007) and joint inversion of receiver function and surface waves (Liu et al. 2014; Sun et al. 2014). However, in most cases, the models from different studies are not consistent with each other, especially in the LMSF zone (Zhang et al. 2012; Wang et al. 2009, 2015; Liu et al. 2014).

In this study, we aim at conducting the first joint inversion of body- and surface-wave data to resolve a more reliable velocity model in the SE margin of the TP. Because two data types are complementary to each other, the joint inversion is able to reduce the non-uniqueness of the velocity model inverted using only a single data type. The body-wave arrival times can better resolve the model in the zones with dense ray coverage and can have good depth resolution. In comparison, the short-period surface-wave dispersion data can provide good resolution in the shallow part of model, where body-wave arrival times generally have poor resolution because of lacking crossing rays (Zhang et al. 2014). In addition, surface waves extracted from ambient noise analysis are not dependent on

the distribution of earthquakes. By using the jointly inverted velocity model, we hope to elucidate the structural features of the aftershock gap and further to explain why the gap exits and understand the earthquake generation mechanisms in this area.

2 Data and method

For the joint inversion, we used two data sets: the first arrivals of P and S waves and dispersion curves for Rayleigh waves. For the body waves, we obtained 65,525 P- and 36,866 S-wave first arrival times from 7190 events recorded by 102 stations for the period of 2001–2004, and from May to August 2008 and April to May 2013 in the SE margin of the TP (Fig. 1). These selected arrival times are carefully checked to follow the major trend of travel-time curves (Fig. 2). From these absolute arrival times, we also constructed 362,105 P- and 231,609 S-wave differential times. Rayleigh wave dispersion curves at periods from 4 to 40 s are extracted from ambient seismic noise data recorded by the densely deployed array, containing 298 broadband seismometers with average inter-station distance of about 15 km in the SE margin of the TP (Huang 2014; Liu et al. 2014). The phase velocity maps for Rayleigh waves from Huang (2014) are shown in Fig. 3. These maps show the basic velocity variation patterns of the study area. At short periods, the Sichuan basin is a low-phase velocity region indicating thick sediments, whereas the SE margin of the TP shows high-velocity anomalies, which are related to Songpan–Garze flysch (Burchfiel et al. 2008). In comparison, at longer periods, the Sichuan basin is associated with high-velocity anomalies, suggesting cold and rigid Yangtze Craton and the SE margin of the TP shows obviously low-velocity anomalies. It is clear that the boundary between the high- and low-velocity zones follows the LMSF in both short and long periods in the SE margin of the TP.

We jointly invert surface-wave dispersion data and body-wave arrival times using the new joint inversion method of Zhang et al. (2014), which combines the regional-scale version of double-difference (DD) tomography algorithm (tomoFDD) and surface-wave inversion. DD tomography can use both absolute times and more accurate differential times to relocate earthquakes and invert velocity models simultaneously (Zhang and Thurber 2003). TomoFDD uses a finite-difference travel-time algorithm and can calculate travel times and ray paths in the spherical earth that is converted into a Cartesian grid system (Zhang and Thurber 2006). LSQR (Paige and Saunders 1982) is used to solve the system of equations. Damping and first-order spatial smoothing are applied to regularize the inverse problem.
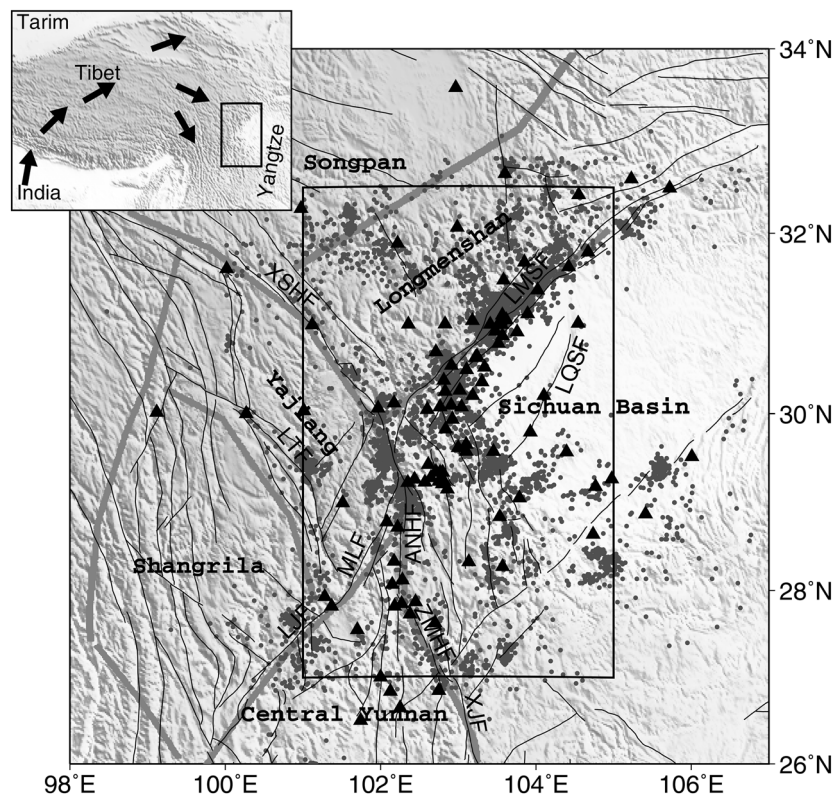
Fig. 1 Map of the SE margin of the TP. Stations (*black triangles*) and earthquakes (*gray dots*) used in this study and faults (*black lines*) overlaid on a topographic map of the SE margin of the TP. *Gray lines* show block boundaries from GPS observations (Shen et al. 2005). The *black box* shows the location of the study area. *Inset*: the *black arrows* represent the approximate surface motion relative to the south China block (Shen et al. 2005). The *black box* shows the location of the study area. Acronyms: *LMSF* Longmenshan fault, *XSHF* Xianshuihe fault, *LTF* Litang fault, *MLF* Muli fault, *LJF* Lijiang fault, *ANHF* Anninghe fault, *ZMHF* Zemuhe fault, *XJF* Xiaojiang fault
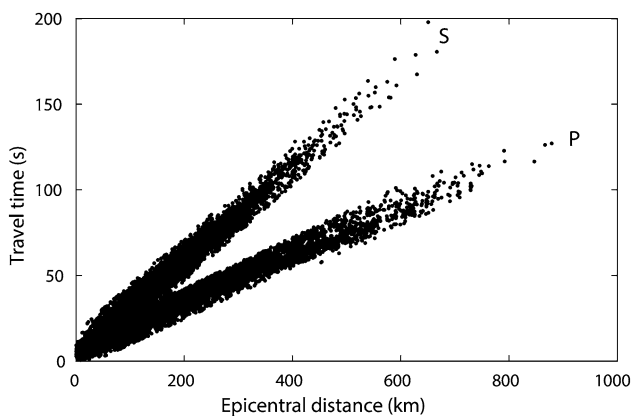
**Fig. 2** P and S travel-time curves

Compared with only body-wave inversion which does not have a good resolution in the shallow part of the crust, the v_S model constrained by body-wave arrival times and surface-wave dispersion data can be more accurate because short-period surface waves are sensitive to shallower crustal structures (Yao et al. 2008). In the traditional surface-wave inversion, v_P model can be obtained from v_S model by postulating a constant v_P/v_S or according to

empirical formulas to calculate the dispersion curves (Li et al. 2009). Instead, in the joint inversion, the v_P model inverted by body-wave times can be directly used to calculate the dispersion data, and therefore, the v_S model inverted by joint inversion is more reliable.

3 Inversion details and model resolution analysis

A three-dimensional (3D) velocity model was inverted based on a minimum one-dimensional (1D) velocity model from the regional 1D velocity model of Zhao et al. (1997). The inversion grid intervals are 0.5° in both latitude and longitude. And in the depth direction, the inversion grid nodes were placed at 0, 5, 10, 17.5, 25, 35, 45, 65 and 90 km, respectively.

The damping and smoothing parameters used to regularize the inversion system as well as the relative weighting between body-wave and surface-wave data are carefully selected by the following processes. Firstly, we determined the optimal damping and smoothing parameters for the inversion system with only body-wave data through a trade-off analysis (Aster et al. 2013). The same damping
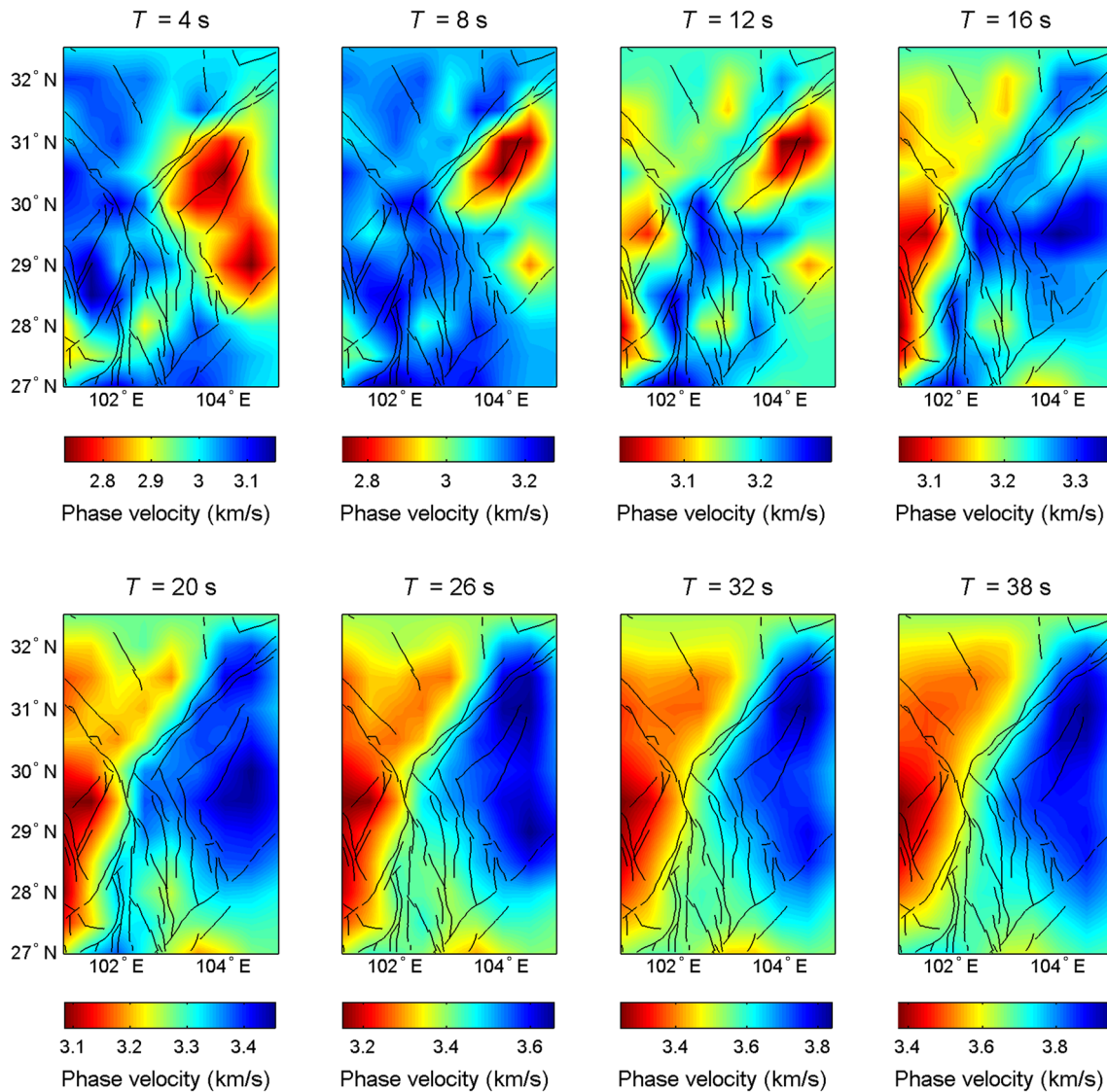
Fig. 3 Phase velocity maps for the Rayleigh waves at 4, 8, 12, 16, 20, 26, 32 and 38 s

and smoothing parameters are applied to the inversion parts related to v_P and v_S. The final absolute P- and S-wave travel-time root mean square (RMS) residuals from only body-wave inversion are 0.218 and 0.298 s, respectively. Based on the selected optimal damping and smoothing parameters, we then select the optimal data weighting parameter to balance surface- and body-wave contributions to the joint inversion objective function. We keep the body-wave weight fixed at 1 and change the surface-wave weight in the range 1–100 because the number of the surface-wave dispersion data is less than that of the body waves. Based on the trade-off analysis, the optimal body- and surface-wave data weights are selected as 1 and 10, respectively. Using these optimal parameters, we obtained the final v_P and v_S models that reduced the absolute body-wave travel-time RMS residual from 1.286 to 0.239 s, an 81%

reduction, and surface-wave dispersion data error from 0.130 to 0.018 km/s, an 86% reduction. Specifically, in the joint inversion, the absolute P-wave travel-time RMS residual is reduced from 1.324 to 0.213 s and from 2.377 to 0.295 s for S-wave arrival times, which are around the same level as the separate body-wave-only inversion. The histograms of P- and S-wave travel-time residuals corresponding to the initial models, and the velocity models obtained by body waves only and by joint inversion are shown in Fig. 4. We can see that travel-time residuals from body-wave-only inversion and joint inversion are more concentrated near 0 s than those corresponding to the initial models.

For Rayleigh wave dispersion data fitting, it can be seen that the RMS residuals for the dispersion data at most of inversion nodes are small (~0.003–0.02 km/s) except for
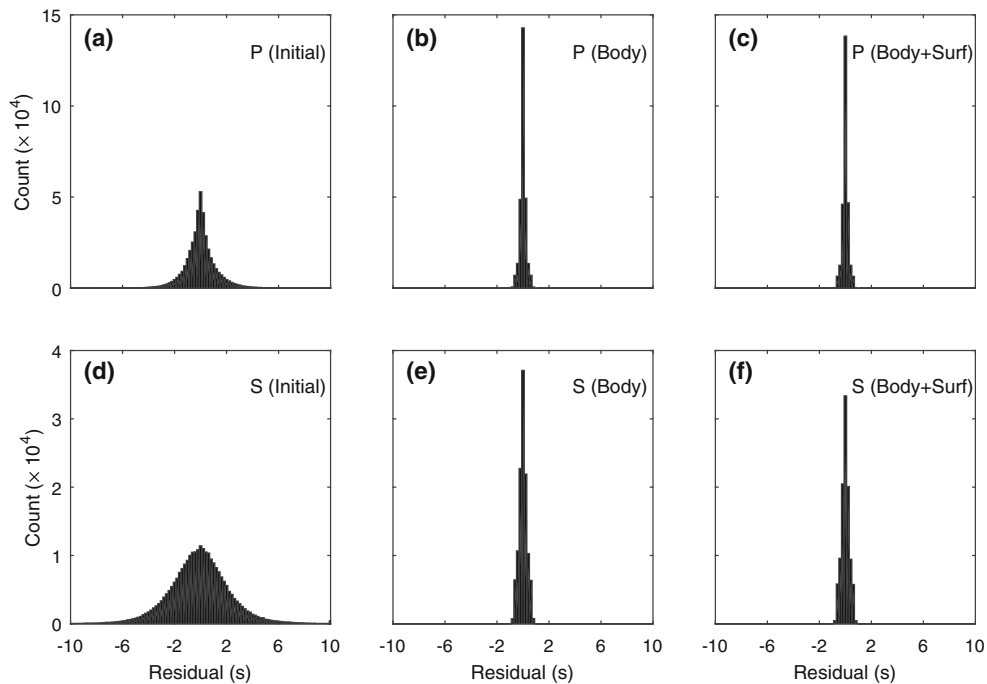
Fig. 4 Histograms of (*top*) P-wave and (*bottom*) S-wave arrival time residuals for different models. **a** and **d**: Initial model; **b** and **e**: Body-wave-only inversion; **c** and **f**: Joint inversion. Residual misfits for velocity models obtained from body-wave inversion only and from joint inversion are more concentrated near 0 s than those related to the initial model

some inversion nodes (∼0.05 km/s) (Fig. 5). At some selected inversion nodes, the Rayleigh wave dispersion curves calculated using the velocity model inverted from joint inversion can fit those obtained dispersion curves from ambient noise tomography very well (Fig. 6). In comparison, the predicted dispersion curves according to the velocity model inverted by body-wave data only cannot fit well with those obtained dispersion curves (Fig. 6).

We use the checkerboard resolution test (Aster et al. 2013) as well as the semblance test to evaluate the resolution of the tomography models. For the checkerboard test, we add velocity perturbations of ±5% to the initial model alternately to adjacent grid nodes in three directions and calculate synthetic travel times with the same event-station distribution as in the real data using the perturbed model. Figure 7 shows the horizontal slices of recovered checkerboard patterns at different depths. The semblance test is an alternative way of assessing the model quality. In the semblance test, we first add random variations on the initial 1D velocity model in three dimensions up to ±7.5%. Then we calculate the P-wave, S-wave travel times and surface-wave dispersion curves with the same data coverage as the real data. The synthetic data are then inverted using the same inversion parameters as the real data. This process is repeated for 100 times and we calculate the semblance between the input model and the recovered model based on Zelt (1998). The semblance values for 100 test models are averaged to obtain the semblance
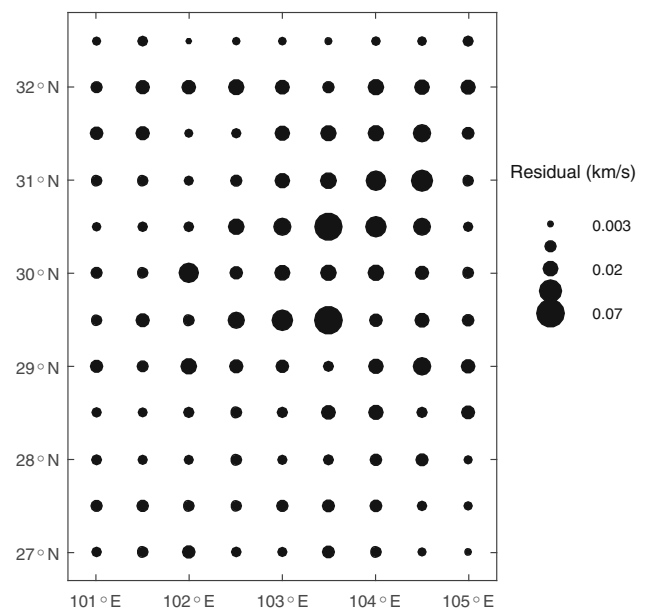
Fig. 5 RMS residuals for Rayleigh wave phase velocity dispersion data at each inversion grid node. The residual scales are shown on the *right*

distribution for the model. A comparison of the semblance distribution of v_P and v_S models for the body-wave inversion only and v_S for joint inversion of body and surface waves is shown in Fig. 8. The regions with semblance values above 0.8 are regarded as well-resolved regions.
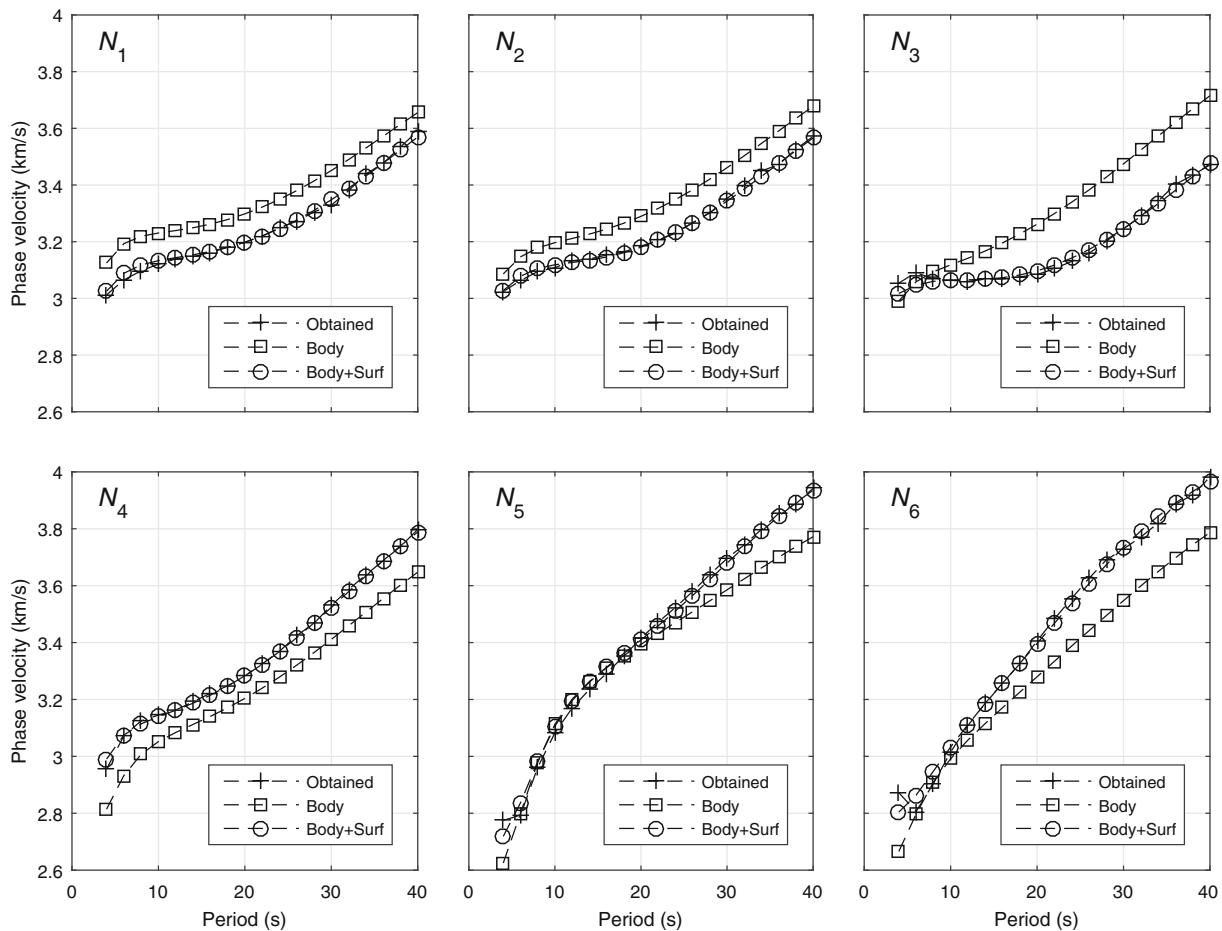
Fig. 6 Comparison of predicted surface-wave dispersion curves from the velocity models inverted using body-wave arrival times only (*square*) and from joint inversion (*circle*) and from real surface-wave dispersion curves (*cross*) at selected grid nodes. The node locations are shown in Fig. 10

The checkerboard test and semblance test results are basically consistent. The two tests indicate that v_P obtained using body-wave arrival times only is well resolved for the model region except for the margin of the study area at each depth (Figs. 7 and 8). However, the checkerboard test shows that the v_S obtained using body-wave data is only well resolved in the central part of the model region down to 17.5 km but is poorly resolved for deeper model zones (Fig. 7) because the ray coverage for S waves is poor in the deeper depths. The v_S obtained using surface waves only is well resolved in the shallow depths, especially at 5 km but have poor resolution at deeper depths (Fig. 7). As expected, the resolution for the v_S model from joint inversion is improved, especially at shallow depths (Figs. 7 and 8). When incorporating the surface-wave data, the outer part and deeper part of the model are better resolved down to depths of 35 km (Figs. 7 and 8). However, at greater depths of 45 and 65 km, the resolution of the v_S model from joint inversion is poorer than that of v_S from only body-wave inversion (Figs. 7 and 8). This may be because

in these deeper depths, the ray coverage of S waves is poor and the surface waves are dominated. Because longer period surface waves have broader depth sensitivity kernels at the deeper region (Yao et al. 2008), the joint inversion cannot resolve such size of grids, resulting in poorer resolutions in the deeper depths.

4 Results

The horizontal slices of the v_P and v_S models inverted from body-wave data only, as well as the v_S model jointly inverted by body- and surface-wave data at 5, 10, 17.5, 25 and 45 km depth are shown in Fig. 9, respectively. The vertical profiles through the velocity models along the lines AA', BB', CC', DD' and EE' are shown in Fig. 10, respectively. The lines AA', BB' and CC' are perpendicular to the LMSF and are through the Wenchuan earthquake, the aftershock gap and the Lushan earthquake from north to south, respectively. The line DD' crosses the gap from the
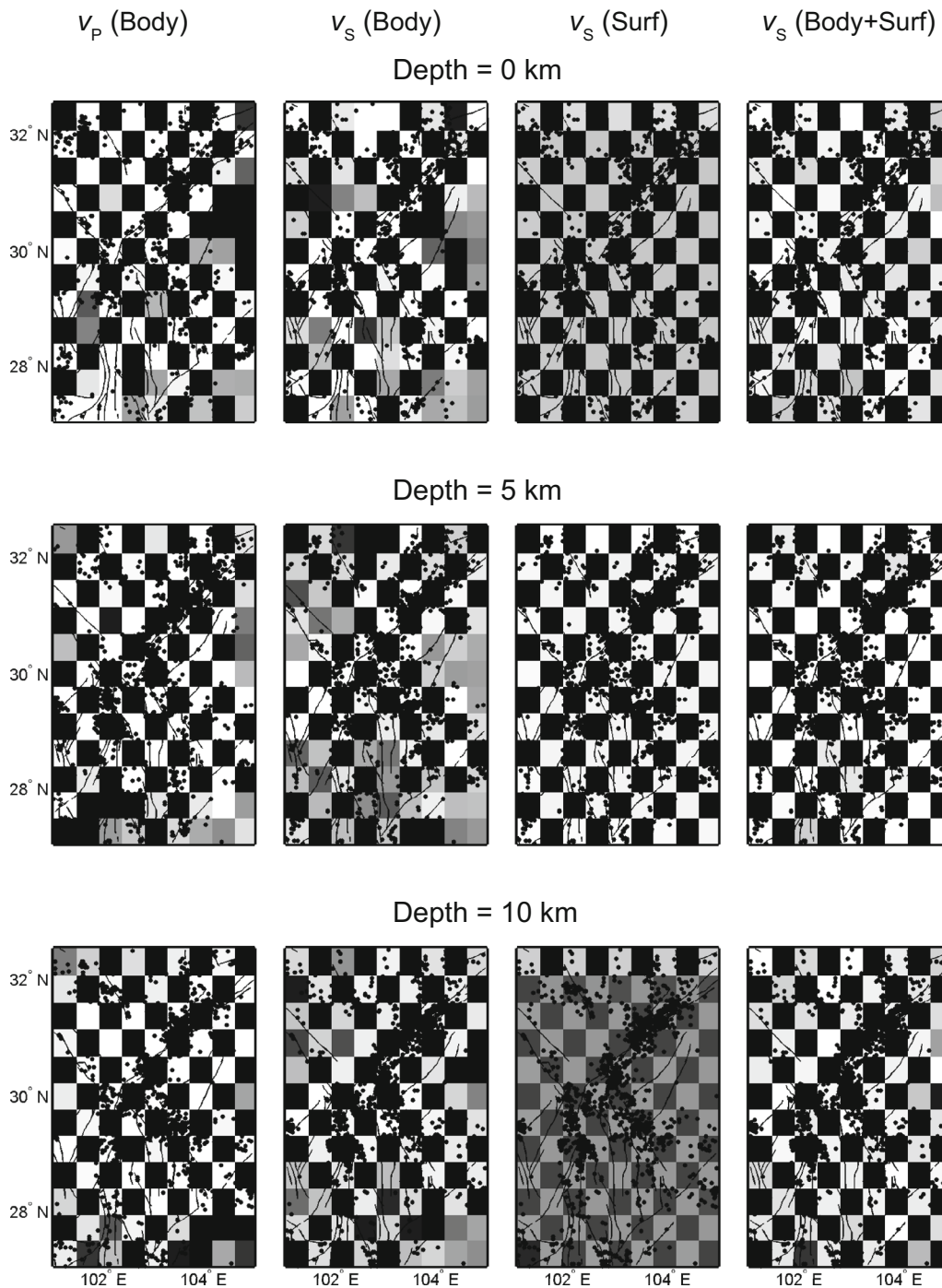
Fig. 7 Recovered checkerboard patterns at each depth for different models. The models are from *left* to *right* are v_P inverted using body-wave arrival times only, v_S inverted using body-wave arrival times only, v_S inverted using surface waves only and v_S jointly inverted by body and surface waves

southwest to the northeast while the line EE' goes along the gentle-topography margin of the SE Tibet.

At shallow depths (5 km), the patterns of velocity anomalies coincide with the local geology (Fig. 9a). For the Sichuan basin, it is clearly associated with low-velocity anomalies, which are caused by primarily Mesozoic and

Paleozoic sediments of >10 km thick in the upper crust (Burchfiel et al. 2008). Among v_P and v_S models inverted separately or jointly, the Quaternary sediments are better delineated by the jointly inverted v_S model (Fig. 9a). Along the LMSF, there exist obvious and variable high-velocity anomalies, which correspond well with the Middle to
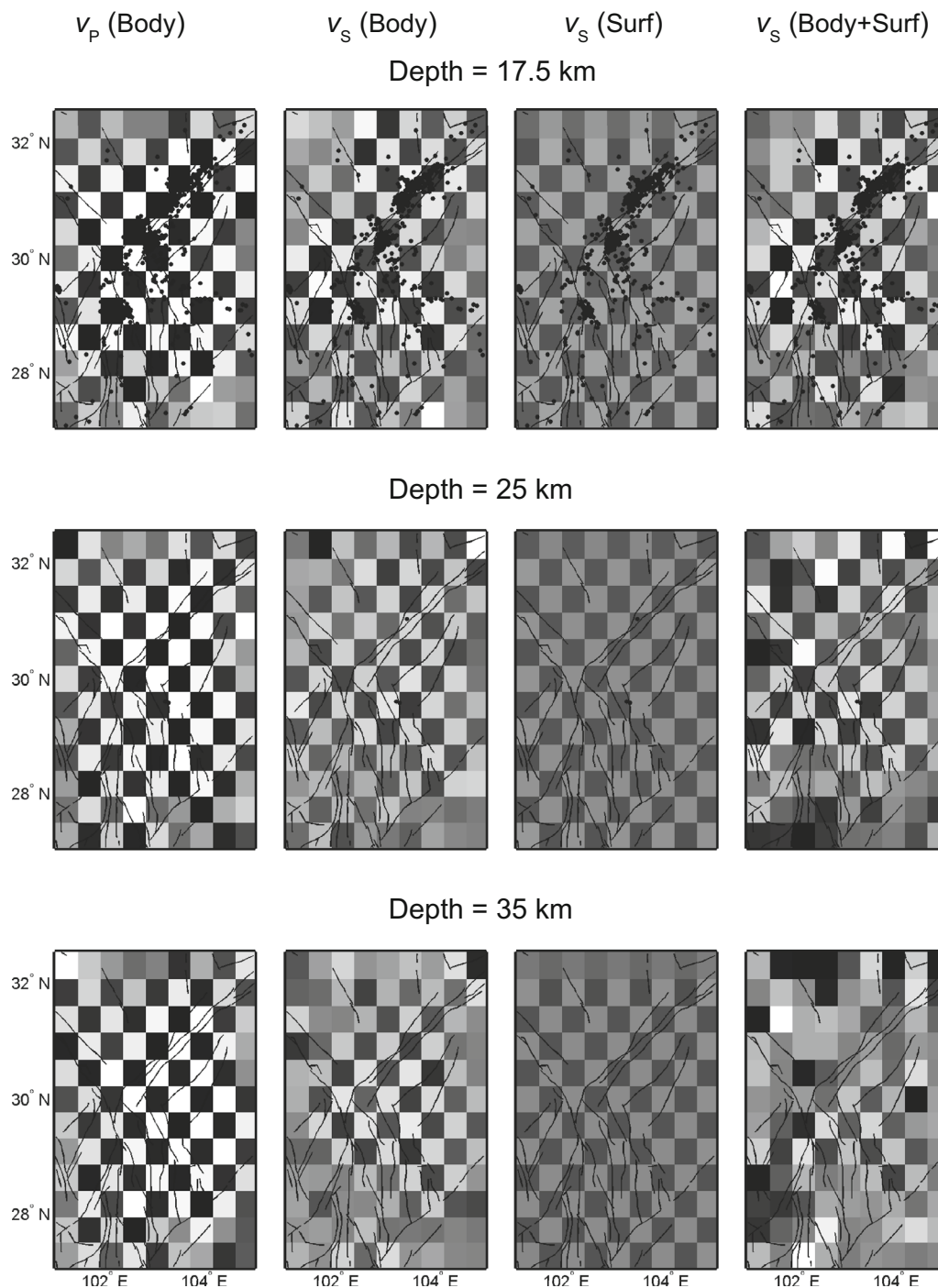
Fig. 7 continued

Upper Triassic flysch with 10 km thick in the LMSF block (Burchfiel et al. 2008). The Yajiang block shows variable and high velocities and the Central Yunnan block shows variable but normal velocities (Fig. 9a).

In the upper crust (10 km), the velocity map shows obvious crustal heterogeneity (Fig. 9b). It is noted that the Sichuan basin is not shown as an overall low-velocity anomaly zone (Fig. 9b). Instead, a high-velocity anomaly

extending parallel to the strike of the LMSF separates two low-velocity anomaly zones from northwest to southeast in the Sichuan basin (Fig. 9b). The Sichuan basin can be divided into three units: the Northwestern Depression, the central uplift and Southeastern Depression (Ma et al. 2007). The Northwestern Depression bounded by the LMSF to the northwest and the Longquanshan fault (LQSF) to the southeast is a foreland basin containing late
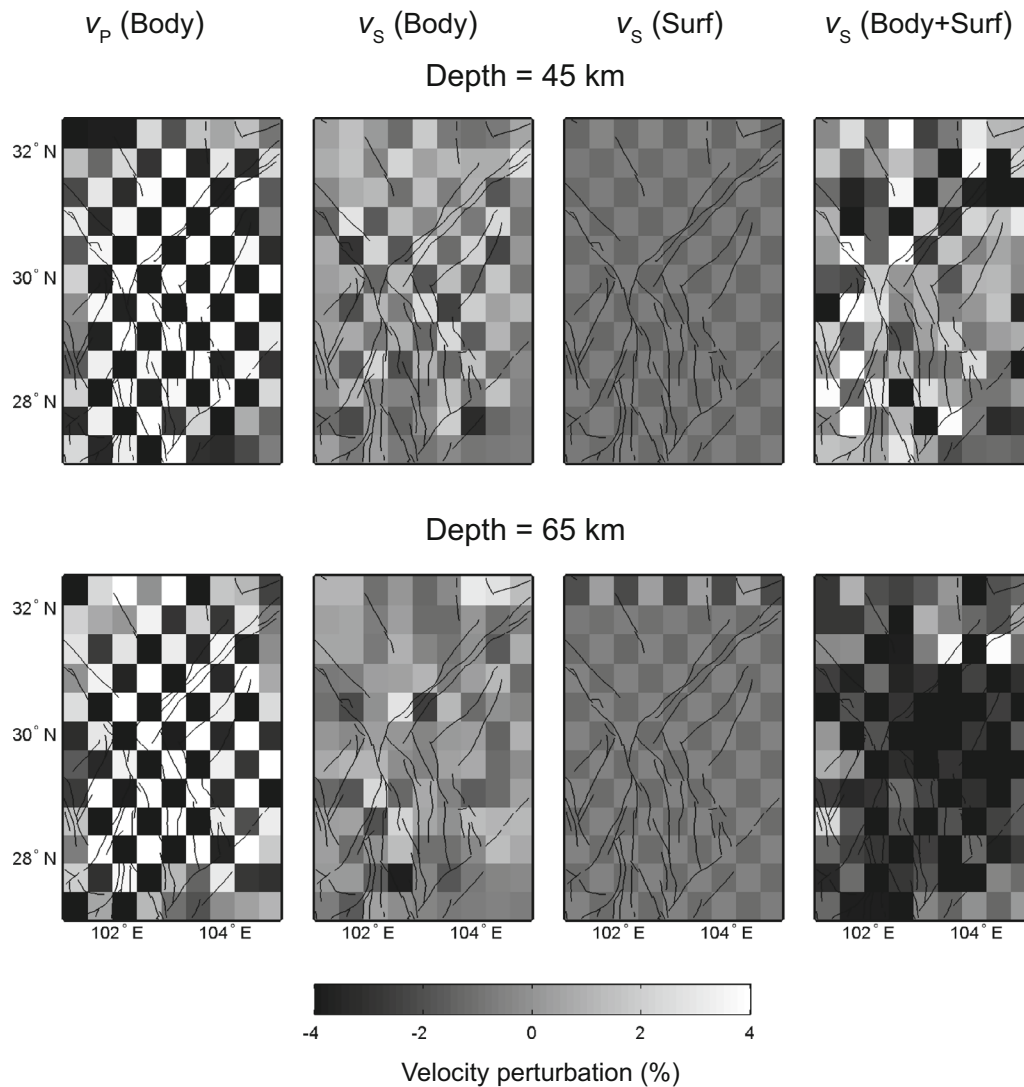
Fig. 7 continued

Proterozoic (Sinian) to Quaternary sediments whose thickness decreases from up to 12 km near the LMSF to about 8 km in the LQSF (Wang et al. 2016). The central uplift bounded by the LQSF to the west and the Huayingshan fault (outside our study area) to the east consists of sediments about 5 km thick (Ma et al. 2007; Wang et al. 2016). In the southern end of Southeastern Depression, the low-velocity anomalies correspond to the sediments of about 10 km thick (Ma et al. 2007; Wang et al. 2016). The velocity anomalies vary in the LMSF, Yajiang and Central Yunnan blocks (Fig. 9b). The high-velocity anomaly in the north of Central Yunnan block at the depth of 10 km (Fig. 9b) is related to the inner core of the Emeishan flood basalt which is caused by materials intruding upwards from the mantle (He et al. 2003). This high-velocity anomaly in the crust is also imaged in previous tomographic studies

(Huang 2014; Liu et al. 2014; Li et al. 2009). In the central part of the study area, our model shows a high-velocity stripe extending southeastwards from the intersection of the LMSF and Xianshuihe fault (XSHF) to the location around longitude 103.5° and latitude 29°. It is also noted that on the depth slices of v_P and v_S models from separate body-wave inversion and joint inversion at 10 km depth, there exist three high-velocity anomaly zones from north to south along the LMSF (HV1, HV2 and HV3 in Fig. 9b). Between these high-velocity zones, there exist low-velocity anomalies along the LMSF (LV1 and LV2 in Fig. 9b).

For the major faults in the study area, they are generally associated with velocity contrasts in the upper crust (Fig. 9a, b). For example, the LMSF is located on the boundary between low velocity in the Sichuan basin and
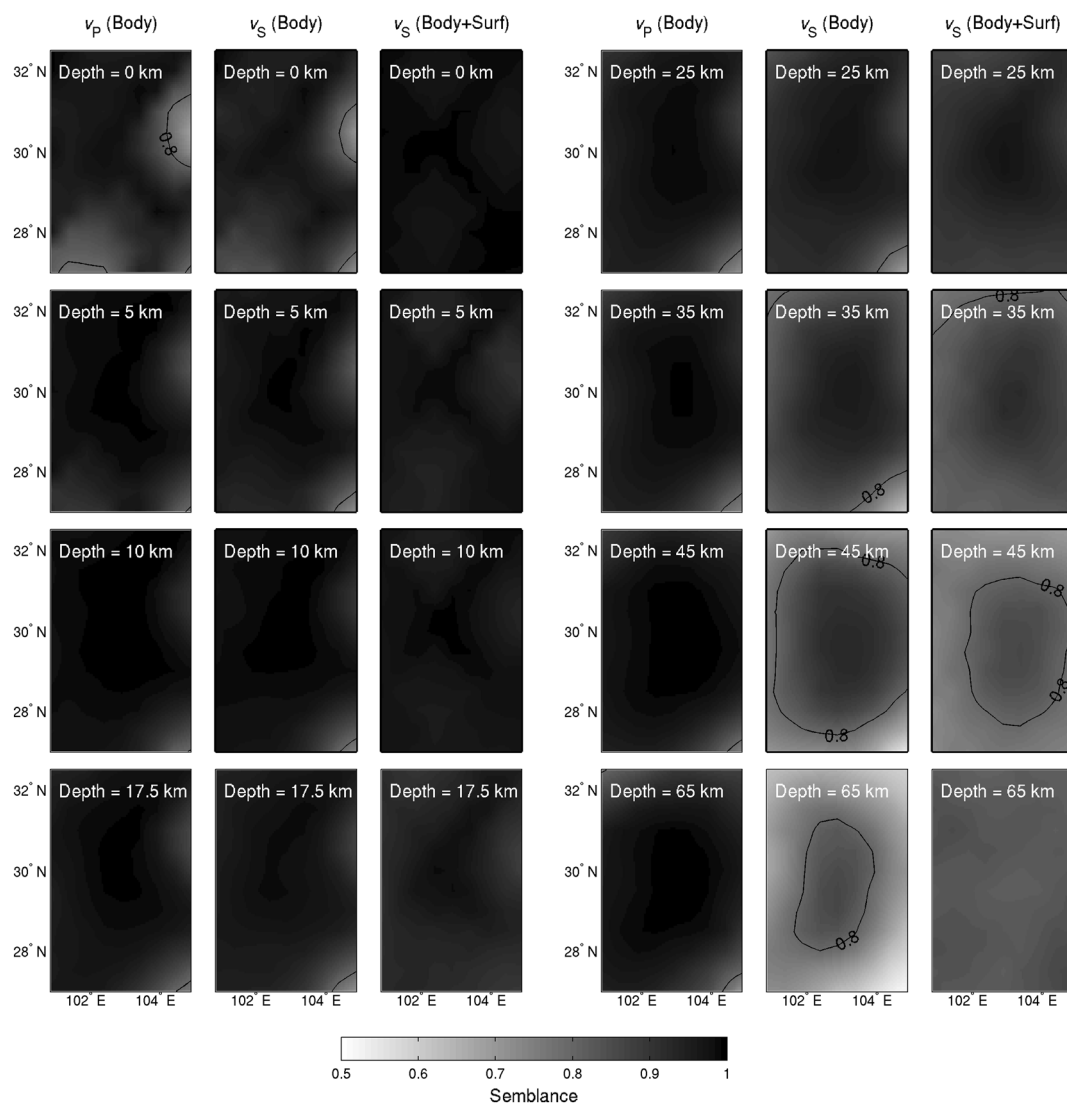
Fig. 8 Horizontal slices of the semblance values for (*left*) v_P and (*middle*) v_S inverted using body waves only and v_S (*right*) jointly inverted by body and surface waves. The contour line indicates the semblance value is 0.8

high velocity in the LMSF block (Fig. 9a, b). Similarly, Xianshuihe, Muli, Anninghe and Zemuhe faults separate low-velocity anomaly on one side and high-velocity anomaly on the other side (Fig. 9a, b).

At the depth of 17.5 km, it is noted that there exist relatively large discrepancies between velocities inverted from separate body-wave inversion and joint inversion (Fig. 9c). In the lower crust (25–45 km), the v_P and v_S models inverted by body waves only are still complex, but the v_S model inverted by joint inversion is simpler and mostly shows large-scale features (Fig. 9d, e). This is because longer period surface waves have larger resolution length (Huang 2014). The v_S model from joint inversion is similar to previous results (Liu et al. 2014; Li et al. 2009) although the checkerboard test shows that the resolution is poorer than that corresponding to body-wave-only

inversion. In the joint inversion v_S model, the most notable feature is the ubiquitous high-velocity anomaly in the Sichuan basin and low-velocity anomaly in the Song-pan–Garze block (Fig. 9d, e), which reflects the cold and rigid craton root to the east and active Cenozoic defor-mation to the west of the LMSF, respectively (Royden et al. 2008).

For the cross sections along profiles AA', BB', CC', DD' and EE' of the joint inversion v_S model, it can be seen that there clearly exist the mid-crustal low-velocity anomalies (Fig. 10). Similarly, the v_P model from separate body-wave inversion also shows low-velocity layers in the middle crust but vague. In comparison, the v_S model from body-wave-only inversion does not show this low-velocity anomaly at all, indicating the v_S model has poorer resolu-tion in this depth range (Fig. 10).
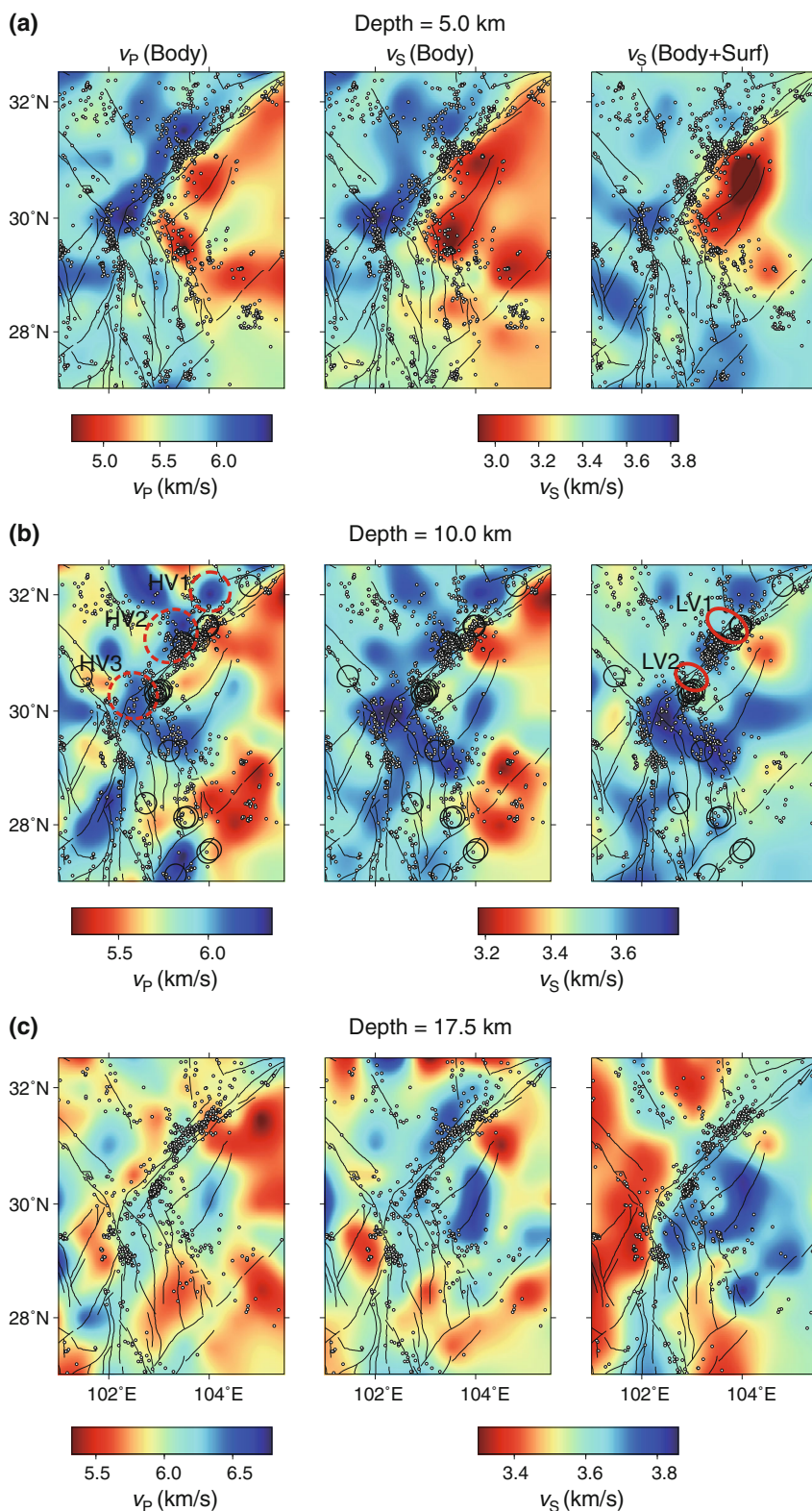
Fig. 9 Horizontal slices of v_P (*left*) inverted by body waves only, v_S (*middle*) by body waves only and v_S (*right*) inverted jointly by body and surface waves at depths of 5, 10, 17.5, 25 and 45 km. The *black circles* at depth of 10 km depict the big earthquakes occurring from 2008 to 2015 in the study area. Three *red dashed ellipses* show three high-velocity patches (HV1, HV2, HV3) along the LMSF and two *red solid ellipses* show the two low-velocity zones (LV1, LV2) in the LMSF zone

(d) Depth = 25.0 km

v_P (Body) v_S (Body) v_S (Body+Surf)

v_P (km/s) v_S (km/s)

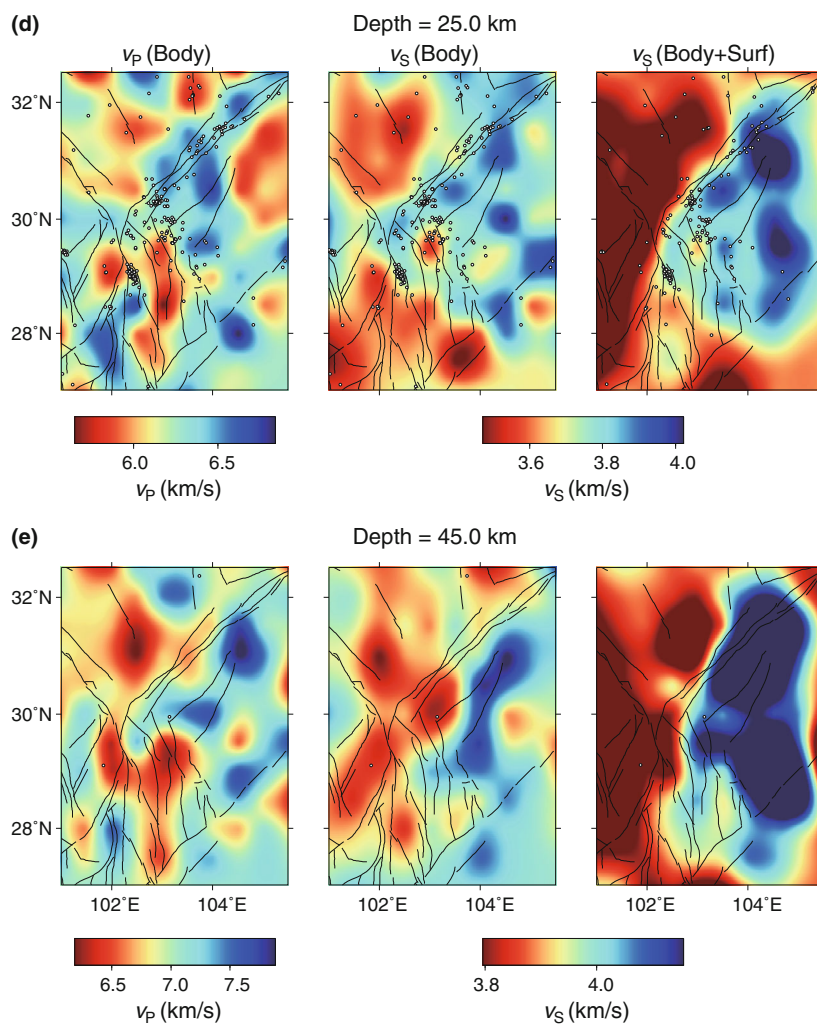**(e)** Depth = 45.0 km

v_P (km/s) v_S (km/s)

Fig. 9 continued

5 Discussion

5.1 The relation between large earthquakes and velocity anomalies

Figure 9b shows the distribution of large earthquakes ($M \geq 5$) that occurred from 2008 to 2015 and velocity variations in the SE margin of the TP. We can see that most large earthquakes occurred around velocity contrasts between the low- and high-velocity zones (Fig. 9b). This phenomenon was also noticed in the previous studies (e.g., Zhao et al. 2002; Mooney et al. 2012). In Japan, it was found that most large earthquakes are generally located along the boundary between the low- and high-velocity zones in the crust and uppermost mantle (Zhao et al. 2002). It was interpreted that in the volcanic areas the low-velocity anomalies are due to high-temperature anomalies caused by magma upward intrusion, and in the forearc

areas under the Japan Islands they are caused by fluids originated from sea water filtration through faults or from slab dehydration (Zhao et al. 2002). In continental regions, it was found that majority of the earthquakes occur around the edges of positive velocity anomalies and a few small magnitude events occur in the regions with positive velocity anomalies (or within continental interior) (Mooney et al. 2012). These studies showed that the process of earthquake generation may be closely related to the velocity distribution or rigidity of the material. The high-velocity zones correspond to stronger blocks and have higher lithospheric strength (rigidity) and a lower strain rate within the seismogenic upper crust (Mooney et al. 2012). As a result, the stress can be more easily accumulated on high-velocity zones, which can thus act as asperities for generation of large earthquakes (Pei et al. 2014). For low-velocity areas, mechanical strength of materials is weak and is not apt to accumulate strain and stress. Around

the velocity contrast between high and low velocities, it is weak and thus the earthquake can be easily nucleated there. This study shows that by determining the detailed velocity structure for one region we may be able to delineate the zones where large earthquakes may occur.

5.2 The relation between the earthquake rupture and velocity distribution

At 10 km depth, along the LMSF, there exist three strong high-v_P and v_S bodies from northeast to southwest (HV1, HV2 and HV3 in Fig. 9b), which correspond to metamorphic rocks of Xueshan plateau, Pengguan Massif, and Baoxing & Kangding Massifs, respectively (Burchfiel et al. 2008; Xu et al. 2008). In particular, the shape and size of the "L-shaped" high-velocity body at the intersection of the LMSF and XSHF coincide well with the Kangding Massif (Burchfiel et al. 2008; Xu et al. 2008). There are two obviously low-velocity anomalies between the three high-velocity bodies along the LMSF zone in the upper crust (LV1 and LV2 in Fig. 9b). The LV2 is situated in the aftershock gap of the Wenchuan and Lushan earthquakes. The LV1 is located from Xiaoyudong to Beichuan where less coseismic slip and fewer aftershocks of the Wenchuan earthquake occurred than the neighboring high-velocity regions (Nishimura and Yagi 2008; Shen et al. 2009). These two low-velocity anomalies are also imaged in the previous tomographic studies (Pei et al. 2010, 2014; Wang et al. 2014, 2015), which mainly consist of Paleozoic marine sedimentary rocks (Burchfiel et al. 2008; Xu et al. 2008). The LV1 is also associated with high-v_P/v_S ratio anomalies (Pei et al. 2010). For the aftershock gap (LV2), two-dimensional Pg imaging revealed that the gap is shown as a low-velocity anomaly (Pei et al. 2014). The 3D velocity model inverted using body-wave arrivals also revealed that the gap is associated with low-velocity and high-conductivity anomalies (Wang et al. 2014, 2015). The two low-velocity anomalies (LV1 and LV2 in Fig. 9b) with high-conductivity or high-v_P/v_S ratio anomalies are weak in mechanical strength and may behave more ductile than the surrounding high-velocity bodies. They could be caused by aqueous or partial molten materials extruded from the lower crust and/or the upper mantle of the eastern Tibet into the crust along the permeable faults in the LMSF (Wang et al. 2015). In the two low-velocity regions, it is hard to accumulate enough stress for large earthquakes to occur. For the aftershock gap, both the 2008 Wenchuan and 2013 Lushan earthquakes did not rupture there. Therefore, this low-velocity zone, with more ductile behavior, may act as barriers for rupturing of both earthquakes. On the other hand, the high-velocity bodies around the Wenchuan and Lushan earthquakes act as asperities for the two earthquakes.

5.3 The distribution of mid-lower crustal low-velocity zones

The mid-lower crustal low-velocity zones (LVZs) are clearly visible in the SE margin of the TP (Figs. 9d, e, 10), which are also imaged in previous studies (Yao et al. 2008, 2010; Li et al. 2009; Yang et al. 2012; Zhang et al. 2012; Liu et al. 2014). These LVZs are also generally associated with high Poisson's ratio (Xu et al. 2007; Wang et al. 2010), high heat flow (Hu et al. 2000) and low electrical resistivity (Bai et al. 2010; Zhao et al. 2012). These anomalies could be caused by partial melt and aqueous fluids in the crust, suggesting that the middle and lower crust in the SE margin of the TP is mechanically weak. The LVZs in the middle and lower crust may be interpreted as the weak mid-lower crustal channel flow (Liu et al. 2014), which might be localized due to the complex 3D geometry of the crustal low-velocity zones (e.g., Yao et al. 2010; Liu et al. 2014). The surface-wave tomography study also showed the strong positive radial anisotropy ($v_{SH} > v_{SV}$) associated with the crustal LVZs (Huang et al. 2010), indicating subhorizontal alignment of crustal minerals, which is consistent with the channel flow model. From the velocity images, it can be seen that the thickness of the mid-lower crustal low-velocity channels varies in the SE margin of the TP (Fig. 10). The LMSF, ANHF and ZMHF mark the main eastern boundary of the LVZs in the middle and lower crust (Fig. 9d, e).

6 Conclusions

New three-dimensional v_P and v_S models are obtained for the SE margin of the TP by joint inversion of the body and surface waves to explore the crustal deformation and earthquake generation mechanism in this region. Compared with separate body-wave-only inversion, joint inversion improves the resolution for the v_S model. At 10 km depth, the three strong high-v_P and v_S bodies along the LMSF are consistent with Precambrian massifs. Two low-velocity anomalies between the three high-velocity bodies along the LMSF are situated in the gap of the Wenchuan and Lushan earthquakes and are associated with less coseismic slip from Xiaoyudong to Beichuan, respectively. The two low-velocity anomalies with high conductivity and high Poisson's ratio imply that the anomaly zones are weak and ductile and thus are hard to accumulate stress enough to cause large slip and earthquakes. The velocity distribution of the Sichuan basin at the depth of 10 km coincides with the thickness of the sediments. The high-velocity anomaly in central Yunnan block at the depth of 10, 17.5 km is related to the inner core of the Emeishan flood basalt. The big earthquakes ($M \geq 5$) occurred in regions between high
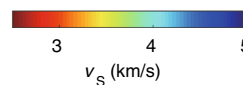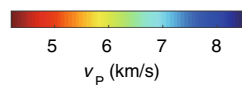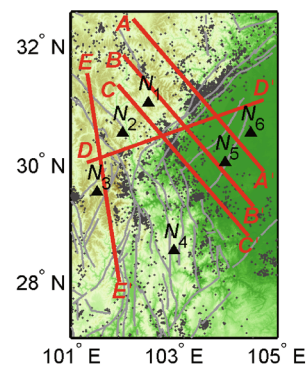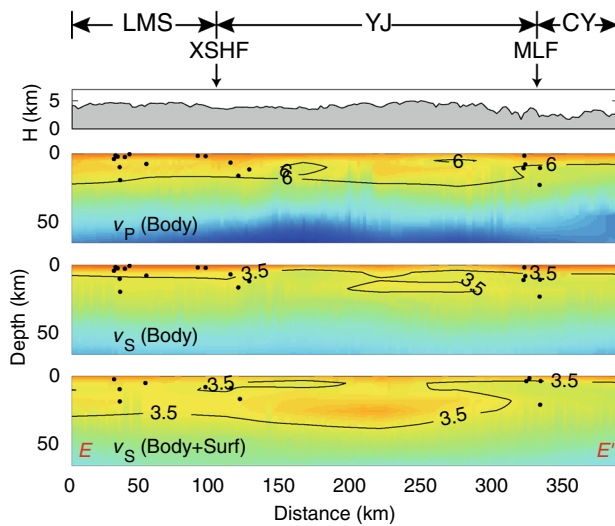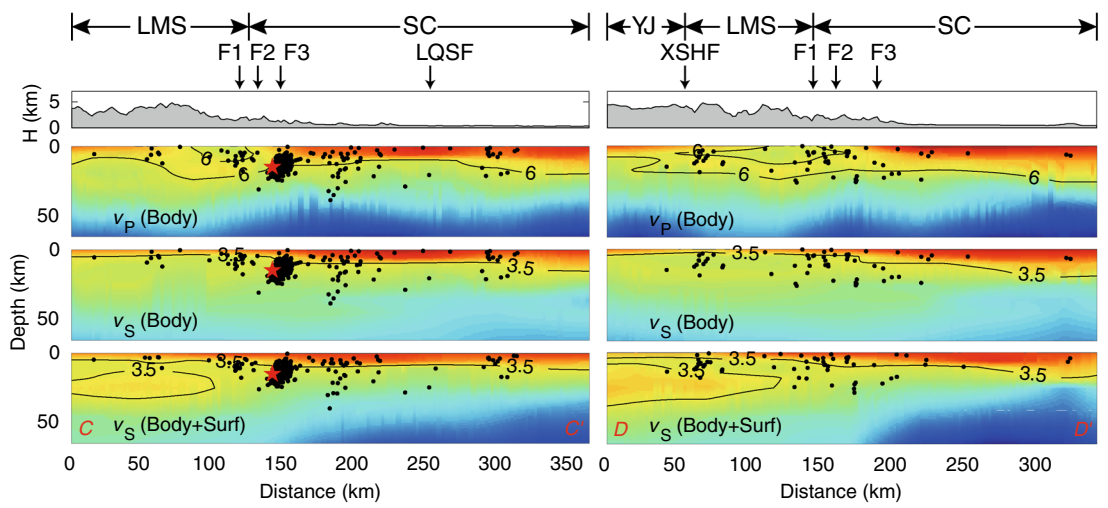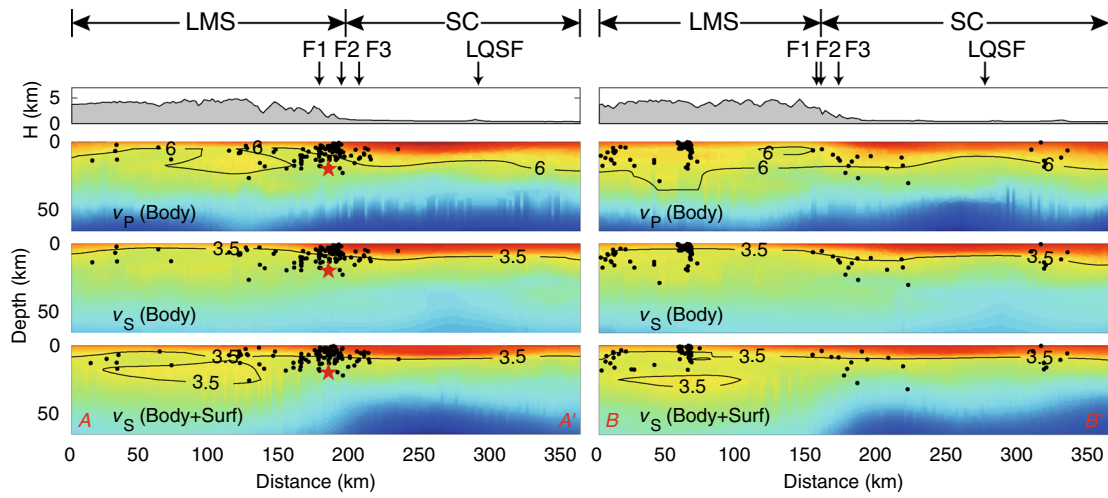
◄**Fig. 10** Vertical cross sections through the (*top*) v_P and (*middle*) v_S models inverted from body waves only and the (*bottom*) v_S model inverted jointly by body and surface waves along the *lines* (A) *AA′*, (B) *BB′*, (C) *CC′*, (D) *DD′* and (E) *EE′*, respectively. The surface topography is shown on the *top* of each profile. *Black dots* represent the relocated earthquakes within 5 km from each profile. *Red stars* in profile *AA′* and *CC′* represent the Wenchuan and Lushan earthquakes, respectively. The profile locations are shown on the *inset* map. The v_P and v_S color scales are shown on the *bottom*. N_1, N_2, N_3, N_4, N_5 and N_6 are node locations shown in Fig. 6. F1: Wenchuan–Maowen fault; F2: Yingxiu–Beichuan fault; F3: Guanxian–Jiangyou fault

and low-velocity bodies, which are the suitable locations to accumulate stress and generate large earthquakes. The low-velocity layers in the mid-lower crust may suggest that the mid-lower crust is mechanically weak, which may facilitate channel flow of crustal materials. However, the distribution of mid-lower crustal low-velocity channel is not homogeneous and is bounded by LMSF, ANHF and ZMHF to the east.

References

Aster RC, Borchers B, Thurber CH (2013) Parameter estimation and inverse problems. Academic, Boston

Bai D, Unsworth MJ, Meju MA, Ma X, Teng J, Kong X, Sun Y, Sun J, Wang L, Jiang C, Zhao C, Xiao P, Liu M (2010) Crustal deformation of the eastern Tibetan plateau revealed by magnetotelluric imaging. Nat Geosci 3(5):358–362

Burchfiel BC, Royden LH, van der Hilst RD, Hager BH, Chen Z, King RW, Li C, Lü J, Yao H, Kirby E (2008) A geological and geophysical context for the Wenchuan earthquake of 12 May 2008, Sichuan, People's Republic of China. GSA Today 18:4–11

He B, Xu Y, Chung S, Xiao L, Wang Y (2003) Sedimentary evidence for a rapid, kilometer-scale crustal doming prior to the eruption of the Emeishan flood basalts. Earth Planet Sci Lett 213(3):391–405

Hu S, He L, Wang J (2000) Heat flow in the continental area of China: a new data set. Earth Planet Sci Lett 179(2):407–419

Huang H (2014) Ambient noise tomography for wavespeed and anisotropy in the crust of southwestern China. Dissertation, Massachusetts Institute of Technology

Huang H, Yao H, van der Hilst RD (2010) Radial anisotropy in the crust of SE Tibet and SW China from ambient noise interferometry. Geophys Res Lett 37:L21310. doi:10.1029/2010GL044981

Lei J, Zhao D (2009) Structural heterogeneity of the Longmenshan fault zone and the mechanism of the 2008 Wenchuan earthquake (M_s 8.0). Geochem Geophys Geosyst 10:Q10010. doi:10.1029/2009GC002590

Lei J, Zhang G, Xie F (2014) The 20 April 2013 Lushan, Sichuan, mainshock, and its aftershock sequence: tectonic implications. Earthq Sci 27(1):15–25. doi:10.1007/s11589-013-0045-9

Li H, Su W, Wang C, Huang Z (2009) Ambient noise Rayleigh wave tomography in western Sichuan and eastern Tibet. Earth Planet Sci Lett 282(1):201–211

Liu Q, van der Hilst RD, Li Y, Yao H, Chen J, Guo B, Qi S, Wang J, Huang H, Li S (2014) Eastward expansion of the Tibetan plateau by crustal flow and strain partitioning across faults. Nat Geosci 7(5):361–365

Ma Y, Guo X, Guo T, Huang R, Cai X, Li G (2007) The Puguang gas field: new giant discovery in the mature Sichuan Basin, southwest China. AAPG Bull 91(5):627–643

Molnar P, Tapponnier P (1975) Cenozoic tectonics of Asia: effects of a continental collision. Science 189(4201):419–426

Mooney WD, Ritsema J, Hwang YK (2012) Crustal seismicity and the earthquake catalog maximum moment magnitude (Mcmax) in stable continental regions (SCRs): correlation with the seismic velocity of the lithosphere. Earth Planet Sci Lett 357–358:78–83

Nishimura N, Yagi Y (2008) Rupture process for May 12, 2008 Sichuan earthquake. University of Tsukuba, Tsukuba, Japan (available at http://www.geol.tsukuba.ac.jp/~nisimura/20080512/)

Paige CC, Saunders MA (1982) LSQR: sparse linear equations and least squares problems. ACM Trans Math Softw 8(2):195–209

Pei S, Su J, Zhang H, Sun Y, Toksöz MN, Wang Z, Gao X, Liu-Zeng J, He J (2010) Three-dimensional seismic velocity structure across the 2008 Wenchuan M_s 8.0 earthquake, Sichuan, China. Tectonophysics 491(1):211–217

Pei S, Zhang H, Su J, Cui Z (2014) Ductile gap between the Wenchuan and Lushan earthquakes revealed from the two-dimensional Pg seismic tomography. Sci Rep 4:6489. doi:10.1038/srep06489

Royden LH, Burchfiel BC, King RW, Wang E, Chen Z, Shen F, Liu Y (1997) Surface deformation and lower crustal flow in eastern Tibet. Science 276(5313):788–790

Royden LH, Burchfiel BC, van der Hilst RD (2008) The geological evolution of the Tibetan plateau. Science 321(5892):1054–1058

Shen Z, Lü J, Wang M, Bürgmann R (2005) Contemporary crustal deformation around the southeast borderland of the Tibetan plateau. J Geophys Res 110:B11409. doi:10.1029/2004JB003421

Shen Z, Sun J, Zhang P, Wan Y, Wang M, Bürgmann R, Zeng Y, Gan W, Liao H, Wang Q (2009) Slip maxima at fault junctions and rupturing of barriers during the 2008 Wenchuan earthquake. Nat Geosci 2:718–724

Sun X, Bao X, Xu M, Eaton DW, Song X, Wang L, Ding Z, Mi N, Yu D, Li H (2014) Crustal structure beneath SE Tibet from joint analysis of receiver functions and Rayleigh wave dispersion. Geophys Res Lett 41(5):1479–1484. doi:10.1002/2014GL059269

Tapponnier P, Peltzer G, Le Dain AY, Armijo R, Cobbold P (1982) Propagating extrusion tectonics in Asia: new insights from simple experiments with plasticine. Geology 10:611–616

Tapponnier P, Xu Z, Roger F, Meyer B, Arnaud N, Wittlinger G, Yang J (2001) Oblique stepwise rise and growth of the Tibet plateau. Science 294:1671–1677

Wang Z, Fukao Y, Pei S (2009) Structural control of rupturing of the M_w 7.9 2008 Wenchuan Earthquake, China. Earth Planet Sci Lett 279(1):131–138

Wang C, Lou H, Silver PG, Zhu L, Chang L (2010) Crustal structure variation along 30°N in the eastern Tibetan plateau and its tectonic implications. Earth Planet Sci Lett 289:367–376. doi:10.1016/j.epsl.2009.11.026

Wang Z, Huang R, Pei S (2014) Crustal deformation along the Longmen-Shan fault zone and its implications for seismogenesis. Tectonophysics 610:128–137

Wang Z, Su J, Liu C, Cai X (2015) New insights into the generation of the 2013 Lushan Earthquake (M_s 7.0), China. J Geophys Res Solid Earth 120:3507–3526. doi:10.1002/2014JB011692

Wang M, Hubbard J, Plesch A, Shaw JH, Wang L (2016) Three-dimensional seismic velocity structure in the Sichuan basin, China. J Geophys Res Solid Earth 121:1007–1022. doi:10.1002/2015JB012644

Xu L, Rondenay S, van der Hilst RD (2007) Structure of the crust beneath the southeastern Tibetan plateau from teleseismic receiver functions. Phys Earth Planet Inter 165(3):176–193

Xu Z, Ji S, Li H, Hou L, Fu X, Cai Z (2008) Uplift of the Longmen Shan range and the Wenchuan earthquake. Episodes 31(3):291–301

Xu X, Wen X, Han Z et al (2013) Lushan M_s 7.0 earthquake: a blind reserve-fault event. Chin Sci Bull 58(28–29):3437–3443. doi:10.1007/s11434-013-5999-4

Yang Y, Ritzwoller MH, Zheng Y, Shen W, Levshin AL, Xie Z (2012) A synoptic view of the distribution and connectivity of the mid-crustal low velocity zone beneath Tibet. J Geophys Res 117:B04303. doi:10.1029/2011JB008810

Yao H (2012) Lithospheric structure and deformation in SE Tibet revealed by ambient noise and earthquake surface wave tomography: recent advances and perspectives. Earthq Sci 25:371–383. doi:10.1007/s11589-012-0863-1

Yao H, Beghein C, van der Hilst RD (2008) Surface wave array tomography in SE Tibet from ambient seismic noise and two-station analysis-II. Crustal and upper-mantle structure. Geophys J Int 173(1):205–219. doi:10.1111/j.1365-246X.2007.03696.x

Yao H, van der Hilst RD, Montagner JP (2010) Heterogeneity and anisotropy of the lithosphere of SE Tibet from surface wave array tomography. J Geophys Res 115:B12307. doi:10.1029/2009JB007142

Yin A, Harrison TM (2000) Geologic evolution of the Himalayan-Tibetan orogen. Annu Rev Earth Planet Sci 28:211–280

Zelt CA (1998) Lateral velocity resolution from three-dimensional seismic refraction data. Geophys J Int 135:1101–1112

Zhang H, Thurber CH (2003) Double-difference tomography: the method and its application to the Hayward fault California. Bull Seismol Soc Am 93(5):1875–1889

Zhang H, Thurber C (2006) Development and applications of double-difference seismic tomography. Pure appl Geophys 163(2–3):373–403. doi:10.1007/s00024-005-0021-y

Zhang Z, Wang Y, Chen Y, Houseman GA, Tian X, Wang E, Teng J (2009) Crustal structure across Longmenshan fault belt from passive source seismic profiling. Geophys Res Lett 36:L17310. doi:10.1029/2009GL039580

Zhang Z, Yuan X, Chen Y, Tian X, Kind R, Li X, Teng J (2010) Seismic signature of the collision between the east Tibetan escape flow and the Sichuan Basin. Earth Planet Sci Lett 292:254–264

Zhang H, Roecker S, Thurber CH, Wang W (2012) Seismic imaging of microblocks and weak zones in the crust beneath the southeastern margin of the Tibetan plateau. In: Dar IA (ed) Earth sciences. InTech Publishing, Shanghai, pp 159–202. ISBN 978-953-307-861-8

Zhang H, Maceira M, Roux P, Thurber C (2014) Joint inversion of body-wave arrival times and surface-wave dispersion for three-dimensional seismic structure around SAFOD. Pure appl Geophys 171(11):3013–3022. doi:10.1007/s00024-014-0806-y

Zhao Z, Fang J, Zhen S (1997) Crustal velocity and relocated events in Longmen Shan fault zone. Acta Seismol Sin 19:615–622. **(in Chinese with English abstract)**

Zhao D, Mishra OP, Sanda R (2002) Influence of fluids and magma on earthquakes: seismological evidence. Phys Earth Planet Inter 132(4):249–267

Zhao G, Unsworth MJ, Zhan Y, Wang L, Chen X, Jones AG, Tang J, Xiao Q, Wang J, Cai J, Li T, Wang Y, Zhang J (2012) Crustal structure and rheology of the Longmenshan and Wenchuan M_w 7.9 earthquake epicentral area from magnetotelluric data. Geology 40(12):1139–1142